www.czasopisma.pan.pl PAN POLSKA AKADEMIA NAUK www.journals.pan.pl

Arch. Metall. Mater. **63** (2018), 4, 1615-1628

DOI: 10.24425/amm.2018.125085

J. WINCZEK*#

THE ANALYSIS OF THERMOMECHANICAL STATES IN MULTIPASS ARC WELD SURFACED STEEL ELEMENTS

The paper presents the analysis of temperature fields, phase transformations, strains and stresses in a cuboidal element made from S235 steel, surfaced with multipass GMA (Gas Metal Arc) method. The temperature field is described assuming a dual-distribution heat source model and summing up the temperature fields induced by the padded weld and by the electric arc. Dependence of stresses on strains is assumed on the basis of tensile curves of particular structures, taking into account the influence of temperature. The calculations were carried out on the example of five welds in the middle of the plate made of S235 steel. The simulation results are illustrated in graphs of thermal cycles, volume shares of structural components and stresses at the selected points of cross-section, and the temperature and strain distributions in the whole cross section.

Keywords: Temperature field, Phase transformation, Gas Metal Arc Weld surfacing

1. Introduction

Welding regeneration or surface hardening processes are frequently performed by multi-pass sequence. In case of multi-pass weld surfacing, the application of subsequent welds causes previous welds to heat up and melt. During subsequent thermal cycles the material in a heat affected zone can undergo multiple phase transformations leading to the diversification of the structure between welds and in the heat affected zone, at the same surfacing parameters. It results in diversified states of strains and stresses in the heat affected zone, as well as outside it.

Modeling of thermomechanical states in the surfacing or rebuilding by welding requires the determination of temperature field. It is necessary to calculate the shares of structural elements taking into account their changes that occur as a result of phase transformations. Finally the thermal and structural strains enable the determination of temporary and residual stresses.

Works refering to thermomechanical state analysis during multi-pass welding, are mainly based on FEM (Finite Element Method) and experimental research. In most publications on FEM techniques for multi-pass welds, a homogeneous model of the material with the thermo-mechanical properties dependent on temperature is adopted and the effect of phase transformation in the solid state is omitted. Lindgren et al. [1] proposed a model of multipass double-sided butt welding of thick plates. The temperature and stress fields were calculated. In experiment transient temperatures and residual stresses were measured at selected points. The agreement between calculations and experiments was good. Jiang et al. in work [2] developed a full 3D thermomechanical FE model, that simulates weld filler material being added continuously with a moving heat source. Numerical simulations were conducted for a butt-welded plate and pipe. Results of calculation with measured temperature and stresses have been compared, obtaining good agreement. 3D thermal model was used by Deng and Murakawa [3] to calculate the temperature field in order to predict internal stresses in multi-pass butt welding (inert and active gas processes) of steel pipes. In the paper the surface model of a heat source with Gaussian distribution was adopted. Jiang et al. [4] estimated the residual stress and deformation in the repair weld of a stainless steel clade plate. The effects of heat input and welding layer number on stresses and deformations have been studied. The authors found that with the welding layer number increase, the residual stresses are decreased. Heinze et al. [5] used a 3D FE model for analysis of the temperature field and stresses during a multi-pass welding of thick structural steel S355J2 under high restraint conditions confirming the experimentally calculated residual stresses. Joshi et al. [6] studied several aspects of evaluating the geometric parameters of Goldak's double ellipsoidal heat source using an experimental case of GMAW (Gas Metal Arc Welding) welding of two overlapping (between 40-80%) beads. Cooling time $t_{8/5}$ and a convective and radiative heat coefficient were calculated. Simulated molten pool and HAZ were compared with experimental macrographs.

There are few works completely modeling thermomechanical phenomena during multipass welding which take into account changeable temperature field, phase transformations as well as stress and strain states connected by a constitutive law. In the work by Börjesson and Lindgren [7] the material model of multipass welding has been extended taking into account mate-

* CZESTOCHOWA UNIVERSITY OF TECHNOLOGY,FACULTY OF MECHANICAL ENGINEERING AND COMPUTER SCIENCE, 21 ARMII KRAJOWEJ STR., 42-201 CZESTOCHOWA, POLAND

Corresponding author: winczek@imipkm.pcz.czest.pl

rial properties dependent on the temperature history. It has been achieved by calculating microstructure evolution and assigning material properties to each phase. Two different materials have been used for the microstructure calculation, one for the base material and one for the filler material. Lindgren and Hedblom [8] presented the complete computational model of the analysis containing special procedure for activation of elements (FEM) at the times when the corresponding parts welds are made. In work [9] an analysis of phenomena of laser welding of steel thin-walled element has been presented. A Comparative analysis of the results of numerical calculations for the dependence of material properties on the temperature, the inclusion of phase transformation in the solid state and the dependence of the yield strength on the phase composition of the material has been made.

In the modelling of the temperature field of welding processes a single-distributed heat source model is generally assumed, reflecting the direct impact of the electric arc on the surfaced object. The shape of the fusion lines during surfacing by welding often exhibit shape irregularity that is difficult to restore by means of the description of the temperature field obtained by using the single-distributed heat source model. In the cited works, as well as in other solutions a single single-distributed heat source model and FEM are used. It is difficult to find work presenting analytical descriptions of thermomechanical states during multi-pass welding (surfacing).

In the paper the analytical models of temperature field, phase transformation kinetics , strains and stresses computations during multi-pass GMAW surfacing are presented. A bimodal heat source model has been used in the description of the temperature field. The model takes into account both the heat of an electric arc directly acting on the object and the heat of the molten electrode material. The adoption of a bimodal volumetric heat source will allow the reconstruction of the irregular shape of the fusion line, which is often found in welding practice and impossible to obtain using a single-distributed heat source. This approach brings model closer to the real phenomena occurring in the welding process. The influence of heat caused by previously padded beads as well as the weld overlap effect have been taken into account in the algorithm. Analytical methods allow rapid assessment of the temperature, shares of structural components, stresses and strains.

2. The model of the temperature field induced by a bimodal heat source

In the description of the temperature field, the bimodal heat source model is presented. The electric arc was treated physically as one heat source, whose heat was divided: part of the heat is transferred by the direct impact of the electric arc, but another part of the heat is transferred to the weld by the melted material of the electrode. This allows of the formulation of the temperature field in the form:

$$T(x,y,z,t)-T_0 = T_a(x,y,z,t)+T_w(x,y,z,t) \tag{1}$$

where $T_a(x,y,z,t)$ and $T_w(x,y,z,t)$ are temperature fields caused respectively by the heat of direct impact of an electric arc and by the heat of the weld reinforcement (consumed to melt the electrode). Analytical description of the temperature field caused by the direct impact of the electric arc with Gaussian heat distribution is shown in [10], whereas considering the heat stored in the liquid metal imposed on the surface is presented in [11]. In the temperature field modeling during multi-pass surfacing it is necessary to take into account temperature increments, caused by overlaying consecutive welding sequences and the self-cooling of areas previously heated and weld overlaps. The temperature field for multipass weld surfacing (Fig. 1) is described by the relationship:

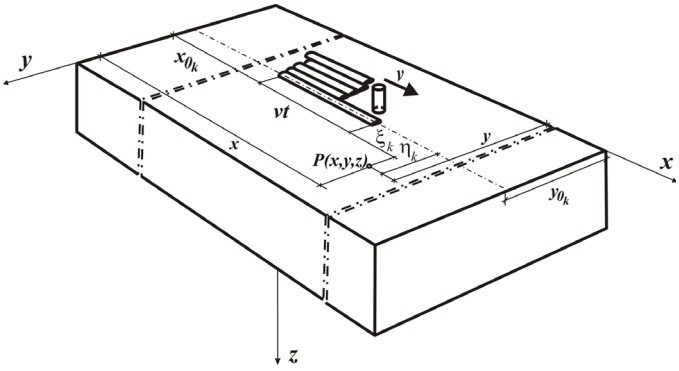

Fig. 1. The scheme of multi-pass weld surfacing: v – velocity of electrode; x_{0_k} – coordinate of of the begining of k-th weld; y_{0_k} – coordinate of k-th weld axis; t – time, that has elapsed since the beginning of surfacing, ξ_k and η_k – distances from considered point of the plate to the position of the electrode

during the application of k-th weld:

$$T(x,y,z,t)-T_0 = \sum_{j=1}^{k-1}\Delta T_j^C + \Delta T_k^H \tag{2}$$

after application of all welds:

$$\phi_A(T) = \sum_j \phi_j^0\left(1-\exp\left(-b_j(T)t^{n_j(T)}\right)\right)+\phi_A^0 \tag{3}$$

where: ΔT_j^C denotes the increment of temperature caused by already applied (cooling) j-th weld, while ΔT_k^H the increment of temperature during application of k-th weld. The algorithm for the temperature field calculation during the multipass surfacing by welding is presented in [12].

3. The description of kinetics of phase transformation in solid state

Kinetics of diffusion transformation is described by JMAK (Johnson-Mehl-Avrami's and Kolomogorov's) rules [13]. The amount of austenite ϕ_A created during heating of the ferrite-pearlitic steel is therefore defined according to the formula [14]:

$$\phi_A(T) = \sum_j \phi_j^0\left(1-\exp\left(-b_j(T)t^{n_j(T)}\right)\right)+\phi_A^0 \tag{4}$$

where ϕ_j^0 constitutes initial share of ferrite ($j \equiv F$), pearlite ($j \equiv P$) and bainite ($j \equiv B$), $\phi_A{}^0$ denotes the amount of residual austenite remaining from the previous welding thermal cycle, while constants b_j and n_j are determined using conditions at the beginning and the end of transformation:

$$n_j = \left[\ln\left(\ln(0.99)\right)\right] / \ln\left(A_1 / A_3\right),\ b_j = 0.01 n_j / A_1 \tag{5}$$

In welding processes the volume fractions of particular phases during cooling depend on the temperature, cooling rate, and the share of austenite (in the zone of incomplete conversion $0 \le \phi_A \le 1$). The progress of phase transformation during cooling is estimated by using additivity rule by volumetric fraction ϕ_j of created phase what can be expressed analogically to Avrami's formula [15] by equation, in which time t is replaced with new independent variable – temperature T [14,16]:

$$\phi_j(T,t) = \phi_A \phi_j^{\max} \left\{1 - \exp\left[b_j(T) t^{n_j(T)}\right]\right\} + \phi_j^0 \tag{6}$$

where:

$$n_j = \left[\ln\left(\ln\left(1-\phi_j^s\right) / \ln\left(1-\phi_j^f\right)\right)\right] / \ln\left(T_j^s / T_j^f\right),$$
$$b_j = n_j \left(1-\phi_j^f\right) / T_j^s \tag{7}$$

ϕ_j^0 is volumetric participation of j-th structural component, which has not been converted during the austenitization, $T_j^s = T_j^s(v_{8/5})$ and $T_j^f = T_j^f(v_{8/5})$ are respectively initial and final temperature of the phase transformation of this component, $\phi_j^{\max}$ denotes the maximal contribution of the phase j, which is then created from the cooled austenite for the determined cooling rate estimated on the basis of the TTT (Time-Temperature-Transformation) welding diagram, while the sum integral volumetric fraction equals 1. The TTT welding diagram binds the time of cooling $t_{8/5}$ (time when material stays within the range of temperature between 500°C and 800°C and the temperature with the progress of phase transformation [14,16].

The fraction of martensite formed below the temperature M_s is calculated using the Koistinen-Marburger formula [17]:

$$\phi_M(T) = \phi_A \phi_M^{\max} \left\{1 - \exp\left[-\mu\left(M_s - T\right)\right]\right\},$$
$$\mu = \ln\left(\phi_M^{\min}\right) / \left(M_s - M_f\right)_j^s \tag{8}$$

where ϕ_M denotes volumetric fraction of martensite, M_s and M_f denote initial and final temperature of martensite transformation respectively, T the current temperature of process and $\phi_M^{\min} = 0.1$.

4. Thermal and structural strains

In the case of multiple actions of the heat source, the total distortion is the sum of thermal and structural strains in the following heating and cooling processes which result from the passage of electrode (a welding head). The total strain during multi-pass welding surfacing represents the sum of thermal strain ε_j^H and structural strain ε_j^C (caused by phase transformations), respectively [18]:

$$\varepsilon(x,y,z,t) = \sum_{j=1}^{k} \varepsilon_j(x,y,z,t) = \varepsilon_j^H + \varepsilon_j^C \tag{9}$$

where ε_j^H and ε_j^C denote the thermal and structural strains during heating and cooling respectively while padding the j-th bead.

Then strains during heating are equal to:

$$\varepsilon_j^H = \varepsilon_j^{Th} - \varepsilon_j^{Trh} \tag{10}$$

where ε_j^{Th} and ε_j^{Trh} are thermal and structural strains, respectively [18]:

$$\varepsilon_j^{Th} = \sum_{i=A,P,F,B,M} \begin{pmatrix} \alpha_i \phi_{i0} \left(T - T_{0j}\right) H\left(T_{A_1} - T\right) + \\ + \alpha_i \phi_i \left(T_{A1} - T_0\right) H\left(T - T_{A_1}\right) + \\ + \alpha_i \phi_i \left(T - T_{A_1}\right) H\left(T_{A_3} - T\right) H\left(T - T_{A_1}\right) + \\ + \phi_i \eta_i \left(T - T_{A_1}\right) H\left(T - T_{A_1}\right) H\left(T - T_{A_3}\right) \end{pmatrix} \tag{11}$$

$$\varepsilon_j^{Trh} = \sum_{i=P,F,B,M} \phi_i \gamma_{iA} \tag{12}$$

where: γ_{iA} – structural strain of i-th structure in austenite, T_0 – initial temperature, α_i – linear thermal expansion coefficient of i-th structure, and $H(x)$ is the Heaviside step function defined as follows:

$$H(x) = \begin{cases} 1 & \text{for } x > 0 \\ 0{,}5 & \text{for } x = 0 \\ 0 & \text{for } x < 0 \end{cases} \tag{13}$$

The strain during cooling can be described by relation:

$$\varepsilon_j^C = \varepsilon_j^{Tc} + \varepsilon_j^{Trc} \tag{14}$$

where ε^{Tc} is the strain caused by thermal shrinkage of material, while ε_j^{Trc} is the structural strain caused by phase transformation during cooling [18]:

$$\varepsilon_j^{Tc} = \alpha_A (T - T_{SOL}) H(T - T_s) + \alpha_A (T_s - T_{SOL}) H(T_s - T) + \\ + \sum_{i=A,P,F,B,M} \alpha_i \varphi_i (T - T_{si}) H(T_{si} - T) \tag{15}$$

$$\varepsilon_j^{Trc} = \sum_{i=P,F,B,M} \eta_i \gamma_{Ai} \tag{16}$$

where T_{SOL} denotes solidus temperature, T_s – the initial temperature of phase transformation, T_{si} – the initial temperature of austenite transformation in i-th structure, $T_s = \max\{T_{sF}, T_{sP}, T_{sB}, T_{sM}\}$, γ_{Ai} – structural strain of austenite in i-th structure. Due to the limit on solid state of material, for temperature exceeding solidus temperature the strain equals 0.

5. Computational model of stress states

The analysis of the stress state was performed for steel rectangular elements whose dimension in the direction of welding dominates over the transverse dimensions. The stress state

of the elements, for which considerations relating to the stress state of rods were used, is approximately uniaxial.

Considered element is exposed to mechanical loads which for particular x cross sections are characterized by the internal forces (sectional) $N = N(x)$, $M_y = M_y(x)$ and $M_z = M_z(x)$. Other sectional forces will be regarded as small (shear forces $T_y = T_y(x)$, $T_z = T_z(x)$), or not occuring ($M_x = M_x(x)$). The element is also subjected to the temperature field $T = T(x,y,z,t)$.

Stress state of the element is characterized by one-dimensional stress state $\sigma_x = \sigma_x(x,y,z,t)$ (Fig. 2), which meets the requirement of the integral equations of stress equilibrium:

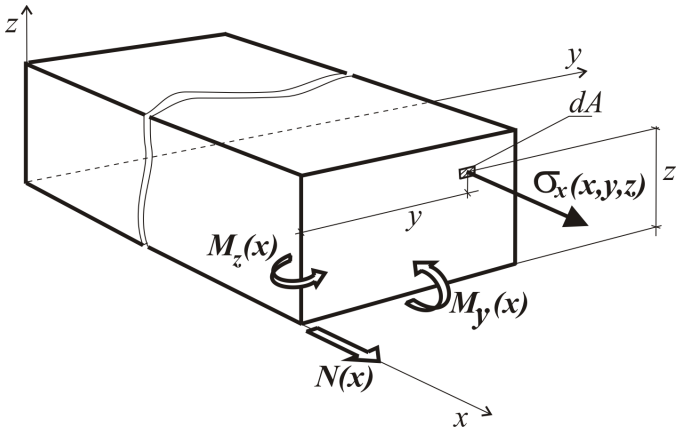

Fig. 2. Scheme of the element subjected to mechanical and thermal loads

$$\begin{aligned}\int_{(A)}\sigma_x dA &= N\\ \int_{(A)}\sigma_x y dA &= -M_z\\ \int_{(A)}\sigma_x z dA &= -M_y\end{aligned} \tag{17}$$

The other three integral equations of equilibrium:

$$\begin{aligned}\int_{(A)}\tau_{xy} dA &= T_y\\ \int_{(A)}\tau_{xz} y dA &= T_z\\ \int_{(A)}\left(-\tau_{xy} z + \tau_{xz} y\right) dA &= M_x\end{aligned} \tag{18}$$

are omitted due to the minimal sectional forces T_y, T_z and M_x.

Cauchy relations were used and the plane cross section hypothesis was adopted in order to introduce stress formulas and element displacements. It was assumed that the cross-sections of the element are subject only to the translation and rotation and do not undergo deplanation or deformations in their plane. The assumption of cross-sectional rigidity of the element in consequence imposes the necessity of proving that linear and angular deformation in the plane are equal to zero. Poisson's ratio also adopts value zero, cross-sections do not respond to lengthening or shortening of the element longitudinal fibers. Displacements of individual cross sections are defined by three translation vectors $u_0 = u_0(x)$, $v_0 = v_0(x)$ and $w_0 = w_0(x)$ at axis x, with x, y and z directions respectively. These displacements are defined as element axial displacement and the element axis deflection in the y and z direction respectively. In the following considerations the geometrical axis of the element is closely related to the axis x. Displacement field of the points that define cross-sections of the element is described by linear dependencies, with the following restrictions:

– displacement field of the element is kinematically allowed (the strains inseparability equations are fulfilled)
– postulated element strain ε_x is small ($\varepsilon \ll 1$).

In the present case, in accordance with technical bendig beam theory, we do not use differential equilibrium equations but only the integral equilibrium equations and the simple Hooke's law $\sigma_x = E\varepsilon_x$, which is equivalent to accepting linear-elastic body in constitutive relations. Therefore:

$$\sigma_x = E\left(u_0' - v_0'' y - w_0'' z - \alpha T\right) \tag{19}$$

and the integral equilibrium conditions (17) will be written in the form:

$$\begin{aligned}\int_{(A)} E\left(u_0' - v_0'' y - w_0'' z - \alpha T\right) dA &= N\\ \int_{(A)} E\left(u_0' - v_0'' y - w_0'' z - \alpha T\right) y dA &= -M_z\\ \int_{(A)} E\left(u_0' - v_0'' y - w_0'' z - \alpha T\right) z dA &= -M_y\end{aligned} \tag{20}$$

Bearing in mind that element axis displacements u_0, v_0 and w_0 are solely the functions of the variable x, under integral values are symbolically saved as:

$$A^E = \int_{(A)} E dA, \quad S_y^E = \int_{(A)} E z dA, \quad S_z^E = \int_{(A)} E y dA,$$

$$J_{yz}^E = \int_{(A)} E y z dA, \quad J_y^E = \int_{(A)} E z^2 dA, \quad J_z^E = \int_{(A)} E y^2 dA,$$

$$N^T = \int_{(A)} \alpha E T dA, \quad M_y^T = \int_{(A)} \alpha E T z dA, \quad M_z^T = \int_{(A)} \alpha E T y dA$$

for elastic modulus which is variable with respect to the coordinates (non-homogeneous element material) or temperature-dependent Young`s modulus, after solving the equations system (20), stresses defined by formula (19) will be written as:

$$\sigma_x = E\left(\left(N + N^T\right)\frac{\Delta_N}{\Delta} + \left(M_y + M_y^T\right)\frac{\Delta_{M_y}}{\Delta} + \left(-M_z + M_z^T\right)\frac{\Delta_{M_z}}{\Delta} - \alpha T\right) \tag{21}$$

where:

$$\Delta_N = J_y^E J_z^E - \left(J_{yz}^E\right)^2 + \left(S_y^E J_{yz}^E - S_z^E J_y^E\right) y + \left(S_z^E J_{yz}^E - S_y^E J_z^E\right) z \tag{22}$$

$$\Delta_{My} = S_z^E J_{yz}^E - S_y^E J_z^E + \left(S_y^E S_z^E - A^E J_{yz}^E\right) y + \\ + \left(A^E J_z^E - \left(S_z^E\right)^2\right) z \tag{23}$$

$$\Delta_{Mz} = S_y^E J_{yz}^E - S_z^E J_z^E + \left(A^E J_y^E - \left(S_y^E\right)^2\right) y + \\ + \left(S_y^E S_z^E - A^E J_{yz}^E\right) z \tag{24}$$

$$\Delta = A^E J_y^E J_z^E + 2 S_y^E S_z^E J_{yz}^E - \left(S_y^E\right)^2 J_z^E \\ - \left(S_z^E\right)^2 J_y^E - A^E \left(J_{yz}^E\right)^2 \tag{25}$$

The stresses in elasto-plastic state are determined by iteration using the method of elastic solutions at the variable modulus of longitudinal elasticity conditioned by the stress-strain curve [19].

6. The example of thermo-mechanical states analysis

6.1. The computations of the temperature field

Computations of changeable in time temperature field, phase transformations and stress states have been conducted for arc weld surfaced quadratic plate with side length 200 mm and thickness 30 mm made from steel S235. Thermal properties of the welded material and the electrode have been determined by $a = 8\times10^{-6}$ m^2/s, c = 670 J/(kg K), $\rho = \rho_e$ = 7800 kg/m^3, ($c\rho$ = 5.2 MJ/mK) i L = 268 kJ/kg.

Numerical simulations of the temperature field during padding of five welds with the length of 100 mm in the middle of the plate (the coordinate of the beginning of welds x_0 = 50 mm) were performed. A heat source with the power 3552 W was adopted, which corresponds to the power obtained with welding parameters: voltage U = 24.3 V, amperage I = 232 A and efficiency η = 0.63. The heat source model for an electric arc with Gaussian distribution of power density is characterized by z_0 = 0.0062 m and t_0 = 0.001 s. In calculations there were assumed: welding velocity v = 0.007 m/s, electrode wire diameter d = 1.2 mm, electrode wire speed v_e = 7.8 m/min, head inclination angle γ = 0 and the weld dimensions: the reinforcement h_w = 2.77 mm and width of the weld w_w = 11.93 mm. I was also assumed that the welding is performed with the use of a semi-automatic welding machine. The execution time of each bead is 28.57 s and time between the welding end one and the beginning next weld is 4 s. The weld overlap is obtained assuming the distance between axes of particular beads equal to 8 mm.

Maximum temperature field in middle cross section (x = 100 mm) is presented in Fig. 3 (for whole cross section) and Fig. 4 (for the middle part of cross section). Critical temperatures isotherms allow to determine the specific heat affected zones. Solidus temperature 1493°C determines the fusion line, whereas the temperatures A_1 = 720°C and A_3 = 835°C determine austenitic transformation zone: partial (between A_1 and A_3) and full (above A_3) – Fig. 5.

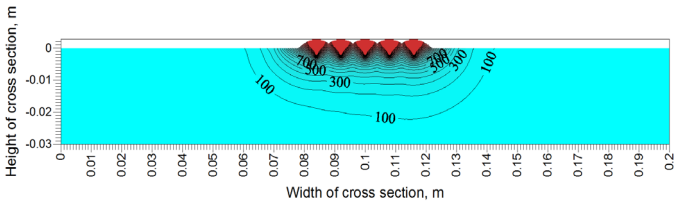

Fig. 3. The field of the maximum temperature in the whole cross section

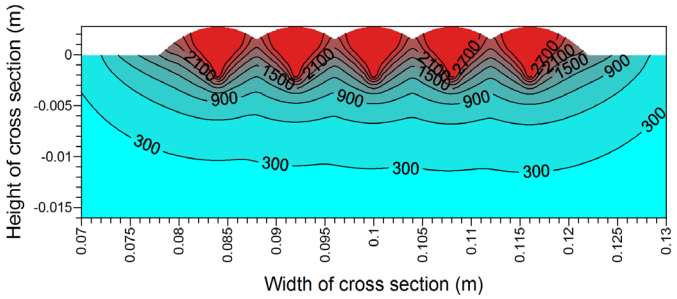

Fig. 4. The field of the maximum temperature in the middle part of cross section

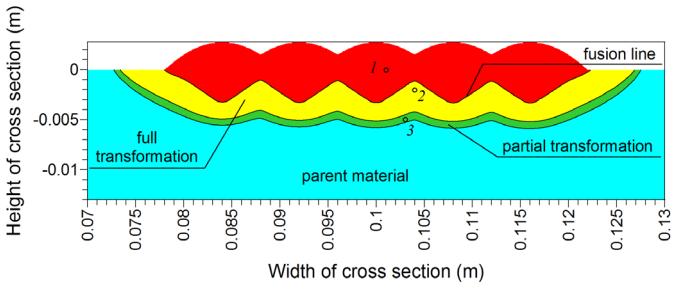

Fig. 5. Heat affected zones

Maximum temperature field shows a slight asymmetry in relation to the longitudinal axis of the welds, material heat-affected zone deepens with successive passages of the electrode. At the same time the fusion depth of individual welds does not show significant differences. However, with the application of successive welds the depth of heat affected zone slightly increases – full and partial austenitic transformation between the first and fifth weld is 0.5 mm, which represents approx. 10% of the distance from the surface of the plate.

In the figure, the selected points of cross section were marked, for which an analysis of welding thermal cycles were performed, and in the following part of the paper – phase transformations, dilatrometric diagrams and stresses. Thermal cycles at points *1-3* are presented in Fig. 6.

In 1-st point, the temperature of the plate material exceeds the austenitizing temperature during the second weld bead, and then the material is melted twice during application of the third and fourth weld. In 2-nd point, the material is not melted, but when making weld bead 3 and 4 it exceeds the temperature of full austenitizing. In 3-rd point, the temperature exceeds the temperature A_1 but does not exceed the temperature A_3, which leads to incomplete austenite conversion during the third weld bead.

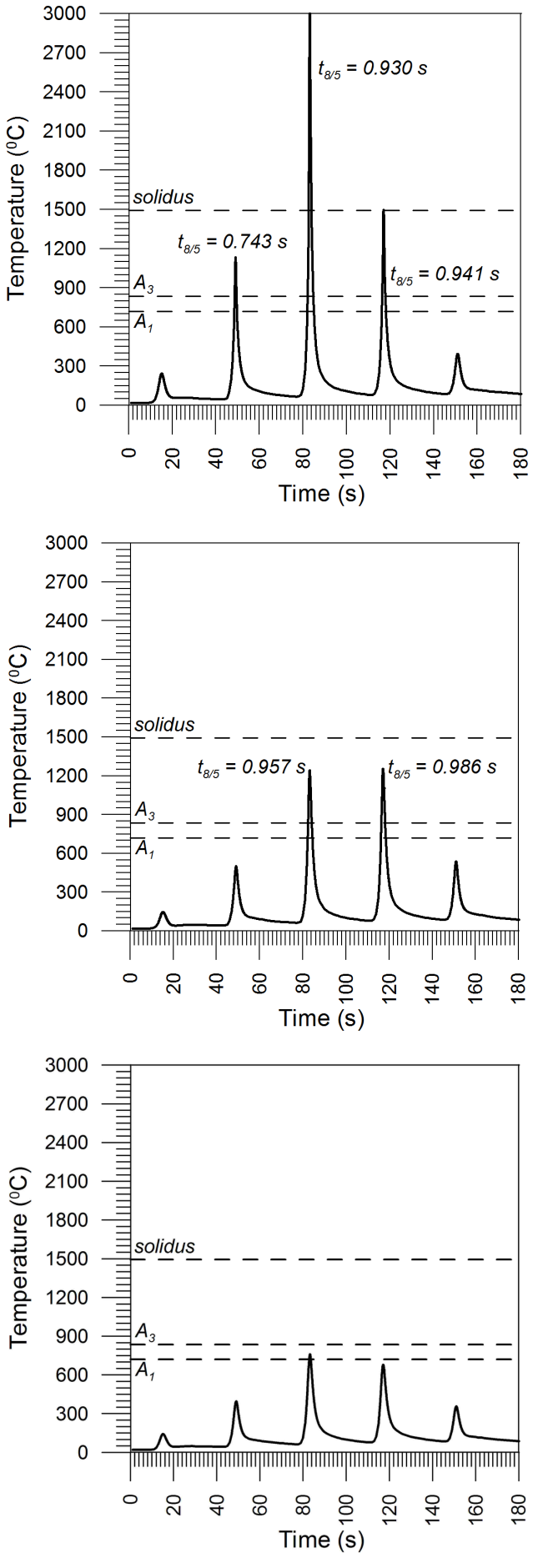

Fig. 6. Thermal cycles at points 1-3

6.2. Simulations of phase share changes and simulations of thermal and structural strains

Kinetics of phase transformation during heating is limited by the initial A_1 and A_3 final temperature of austenitic transformation, whereas the progress of phase transformation during cooling has been determined on the basis of TTT-welding diagram for S235 steel [20] presented in Fig. 7. The applied computational model allows one to determine the shares of the various phases at any point of the body for any chosen time.

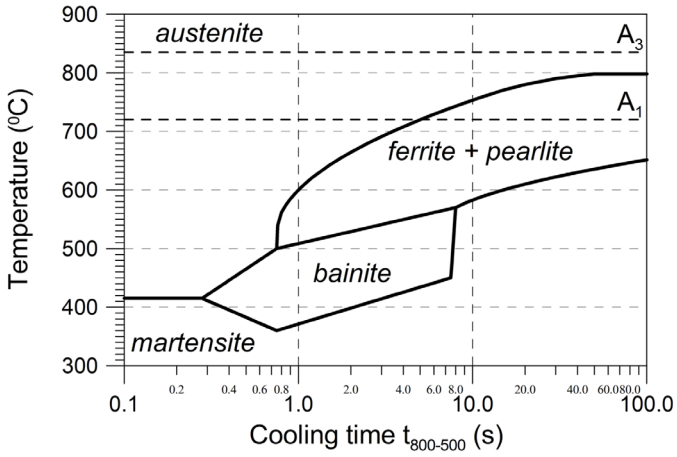

Fig. 7. TTT-welding diagram for S235 steel

The change in phase shares at selected points of the cross section (comp. Fig. 5) is presented in Fig. 9. At point *1* full austenitization and cooling structures formation occurred three times. During the application of the second weld full austenitization occurred and as a result of high speed cooling ($t_{8/5}$ = 0.743 s – comp. Fig. 6.1) 100% bainite was created. During the 3rd and 4th bead full austenitization occurred again (also material melting), but the rate of cooling was then significantly lower ($t_{8/5}$ respectively 0.930 s and 0.941 s), which resulted in formation of 62.3% bainite, 26.4% ferrite and 11.4% pearlite during cooling in the third cycle, and in the fourth cycle 61.9% bainite, 26.7% ferrite and 11.4% pearlite. In point 2 full austenitization occurs twice as well (while performing the third and fourth weld). During cooling the structures with slight variation in volume fraction are formed in the 3-rd and 4-th heat cycles ($t_{8/5}$ respectively 0.957 s and 0.986 s – comp. Fig. 6.2): bainite 61.3% and 60.4%, ferrite 27.1% and 27.7%, pearlite 11.6% and 11.9%. In point 3 the maximum temperature exceeded A1 but did not exceed A3 and as a result there was a partial transformation of the material initial structure into the austenite. During heating 60.5% austenite was formed, which during cooling was converted to bainite (33.7%), ferrite (18.7%) and pearlite (8.1%), which after the addition of participation/share of non-transformed phases gave 46.3% ferrite, 19.9% pearlite and 33.7% bainite.

Figures 9-11 show volume fraction of bainite, pearlite and ferrite after the completion of surfacing process (after material cooling). The percentage of bainite (Fig. 9) amounts in the area of the weld from 63% up to 100% at the interface of plate face

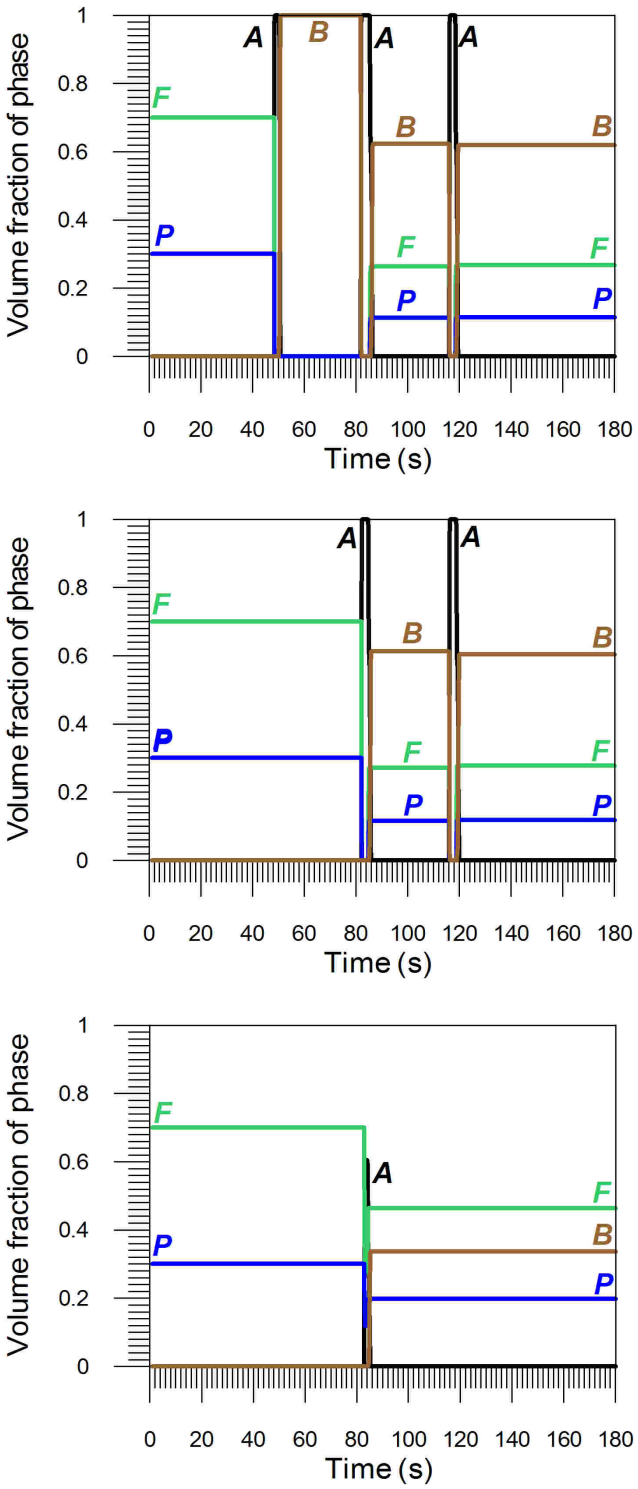

Fig. 8. Phase volume fraction changes at points 1 - 3 of cross section

of the first, second and fifth welds. Overall, the biggest bainite share appears in areas where there has been a single austenitization at relatively high cooling speeds and this share is decreasing deeper in the material. Areas in which the cooling process took place at lower speeds (including those where the performance of successive beads resulted in re-austenitization) revealed the bainite share from 60 to 70%. Pearlite volume fraction (Fig. 10) is up to 12% in full transformation and fusion zones, and grows in incomplete transformation zone up to the value of 30% in the area of parent material. While the ferrite volume fraction (Fig. 11) constitutes 28% of the volume in welds and full transformation zone, and increases to 70% in the parent material zone.

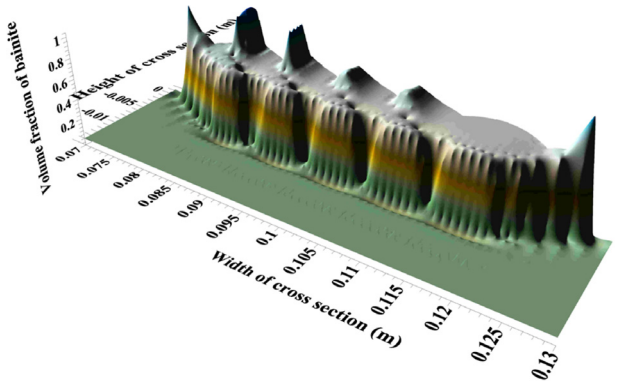

Fig. 9. Volume fraction of bainite after surfacing

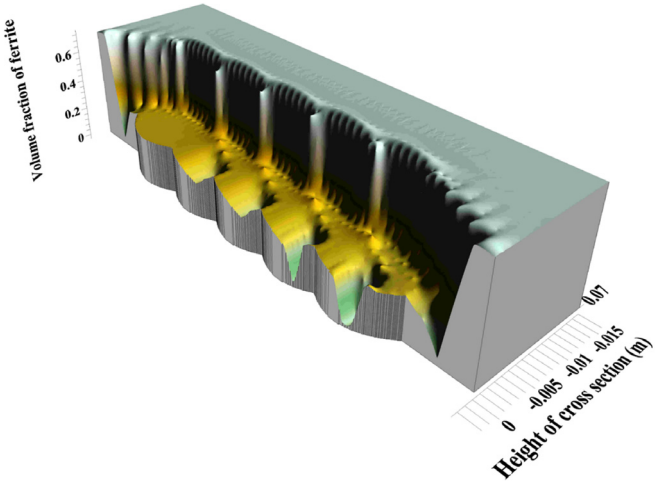

Fig. 10. Volume fraction of ferrite after surfacing

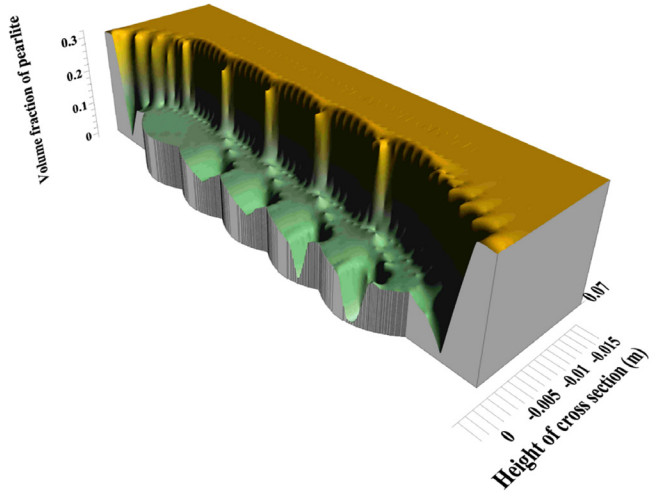

Fig. 11. Volume fraction of pearlite after surfacing

Structural strains resulting from different densities of the individual structures are related to the phase transformations, what in connection with the thermal strains leads to complicated

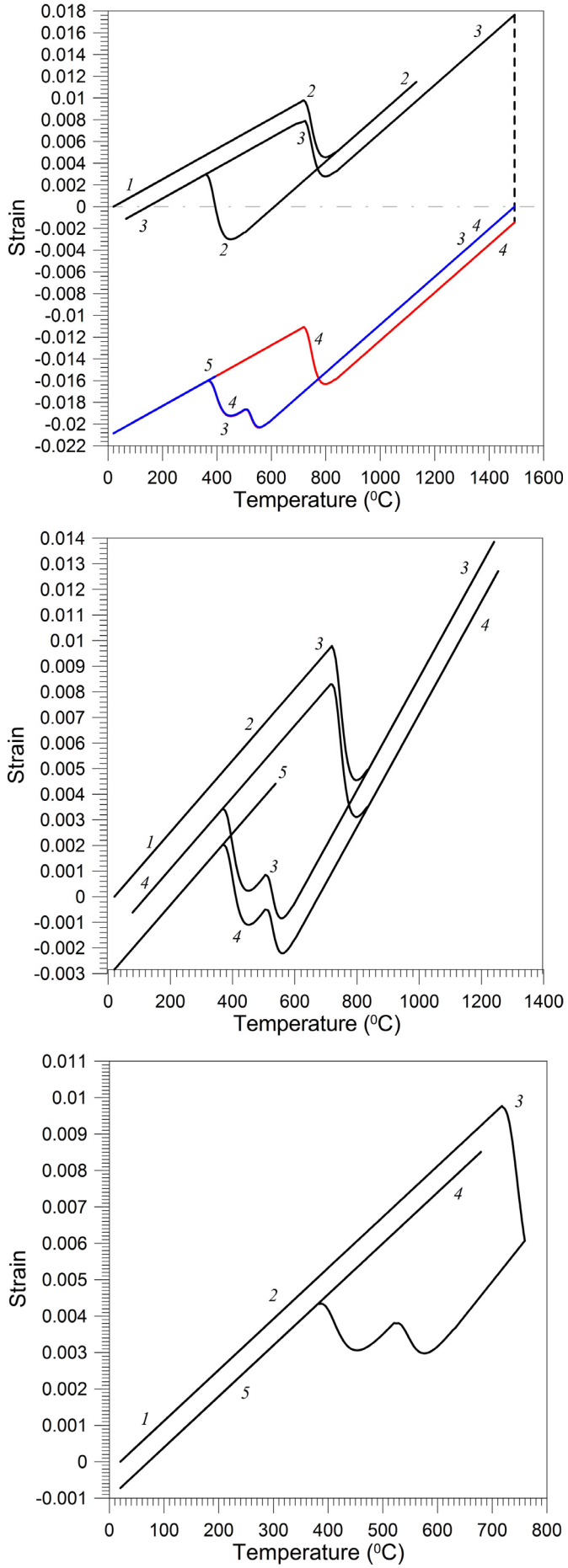

Fig. 12. Dilatometric diagrams 1-3 of cross section [43]

strain history during multiple thermal cycles shown in the form of dilatometric diagrams for selected points of the cross section in Fig. 12. The numbers plotted in the graphs refer to the subsequent thermal cycles connected with overlapping respective welds. In strain calculations there were assumed linear expansion coefficients of particular structural elements and structural stresses (Tab. 1) determined on the basis of the author's own dilatometric research [21].

TABLE 1

Structural (g) and thermal (a) expansion coefficients of phases [42]

	α [1/°C]		γ
Austenite	2.178×10^{-5}	$\gamma_{F,P,S\rightarrow A}$	1.986×10^{-3}
Ferrite	1.534×10^{-5}	$\gamma_{B\rightarrow A}$	1.440×10^{-3}
Pearlite	1.534×10^{-5}	$\gamma_{A\rightarrow F,P}$	3.055×10^{-3}
Bainite	1.171×10^{-5}	$\gamma_{A\rightarrow B}$	4.0×10^{-3}
Martensite	1.36×10^{-5}		

In point *1*, the maximum temperature of the first cycle does not exceed the temperature of the beginning of austenitizing, there was no phase transformations and the graph is rectlinear. In the second cycle, a complete austenitic transformation occurred during heating, and then (in the temperature range 499-360°C) the transformation of austenite to bainite, which is illustrated by a fault in the graph marked with digit *2*. In the third cycle, while heating the complete austenitic transformation occurs (*3*), and then melting (graph fault indicated by a dotted line). After solidification of the material a graph begins at 1493°C (digit *3*) with a rectilinear section (to a temperature of 589°C) reflecting the shrinkage of the material. Cooling transformations are causing faults in the graph to a temperature of 368°C, then a graph again assumes the shape of a straight line. In the fourth cycle a complete transformation and the melting of the material occurs again during heating. After solidification a graph coincides with the line of deformations from the previous cycle until the start of cooling phase transformations, where the lines are slightly shifted relatively to each other. In the fifth cycle phase transformations do not occur, and a graph is rectilinear.

In point *2* of a complete transformation zone (the material has not been melted during the entire surfacing process) a dilatometric graph retains its continuity. In the first two cycles, the temperature does not exceed the initial temperature of austenitization and the graph remains rectilinear. In the third cycle, complete austenitization occurred during heating, whereas during cooling the austenite was converted into the hardening structures, what is visible in the form of characteristic faults on the graph. Similar phenomena occurred in the fourth cycle, the graphs for the third and fourth cycle are clearly shifted. In the fifth cycle, there were no phase transformations and graph retains rectilinear character.

In point *3* the incomplete conversion of austenitic occurred in the third cycle

6.3. The analysis of temporary and residual stresses

Tensile curves of ferrite and pearlite are assumed on the basis of works [22,23]. In case of austenite, bainite and martensite on the basis of data from works [24,25] tensile curves are determined according to Swift law [26]. Stress state analysis was carried out for the middle cross section of the welded plate. Figures 13-22 show normal stress distribution in the considered cross-section at the selected welding times during the process. Whereas Figures 23 and 24 present residual stress distribution after complete cooling of the material.

Plastic strain distribution in the whole cross section is presented in Fig. 25, and the distribution of these strains in the middle part of cross section is shown in Fig. 26. The highest values of plastic strains occur in welds and heat affected zone, especially in areas with the highest bainite volume fraction (comp. Fig. 10).

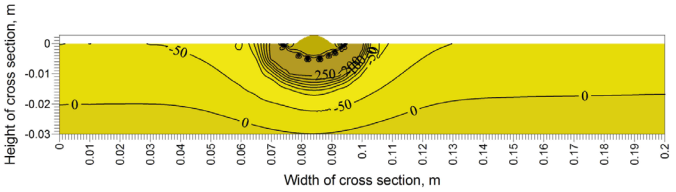

Fig. 13. The stress distribution in the whole cross section after application of 1st weld

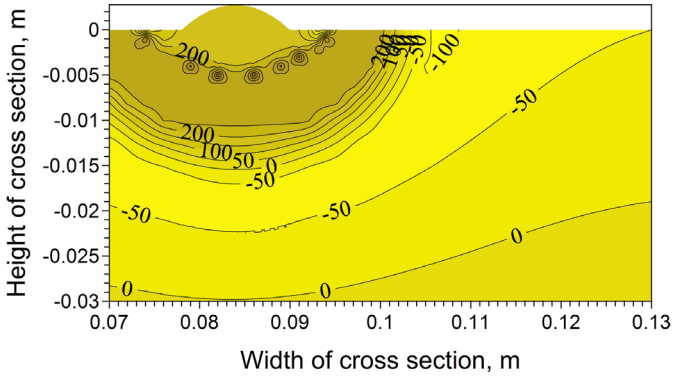

Fig. 14. The stress distribution in the middle part of cross section after application of 1st weld

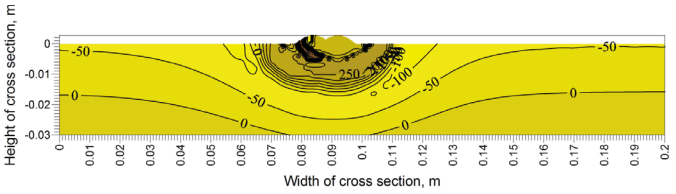

Fig. 15. The stress distribution in the whole cross section after application of 2nd weld

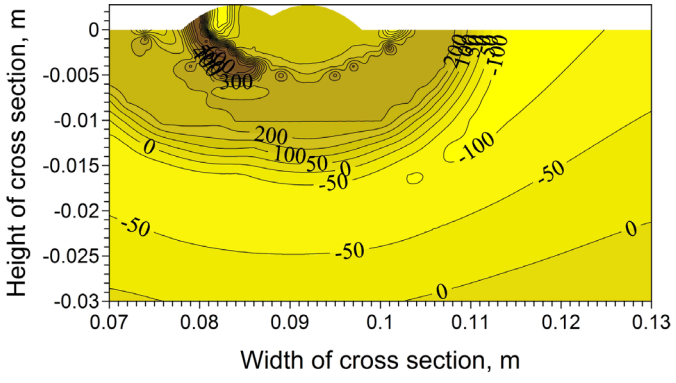

Fig. 16. The stress distribution in the middle part of cross section after application of 2nd weld

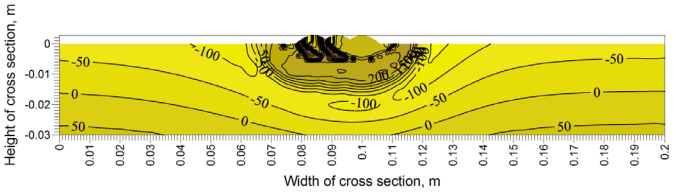

Fig. 17. The stress distribution in the whole cross section after application of 3rd weld

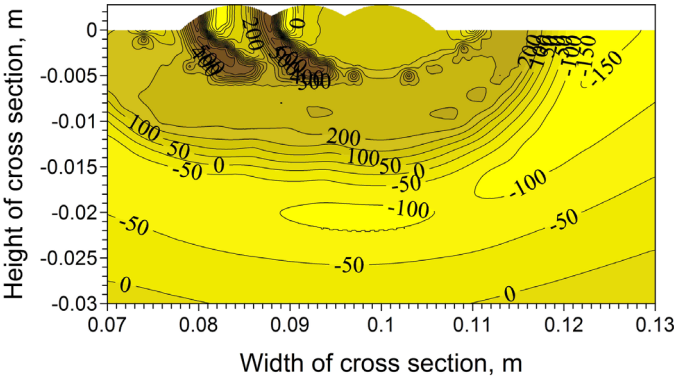

Fig. 18.The stress distribution in the middle part of cross section after application of 3rd weld

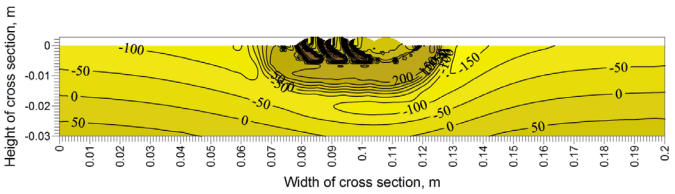

Fig. 19. The stress distribution in the whole cross section after application of 4th weld

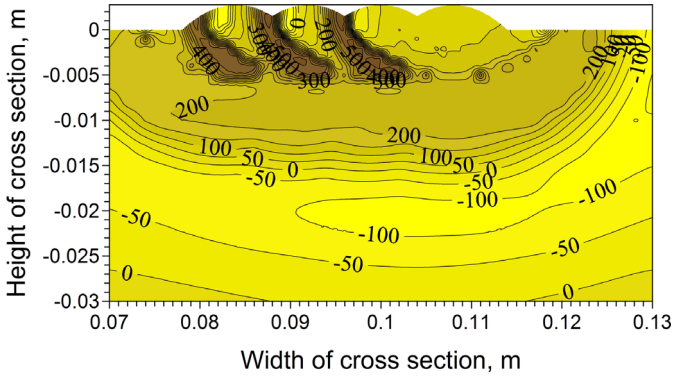

Fig. 20. The stress distribution in the middle part of cross section after application of 4th weld

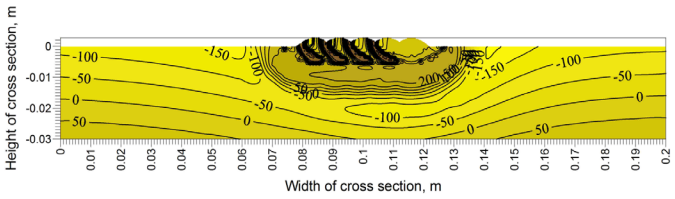

Fig. 21. The stress distribution in the whole cross section after application of 5th weld

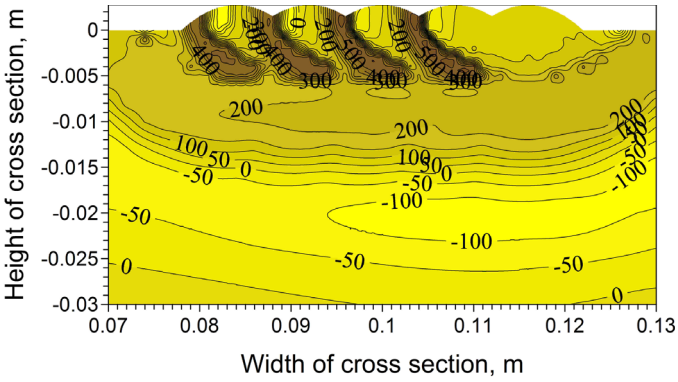

Fig. 22. The stress distribution in the middle part of cross section after application of 5th weld

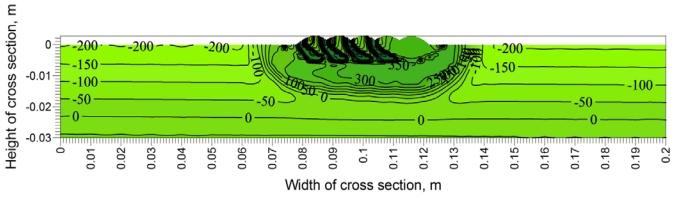

Fig. 23. Residual stress distribution in the whole cross section after the weld cooling

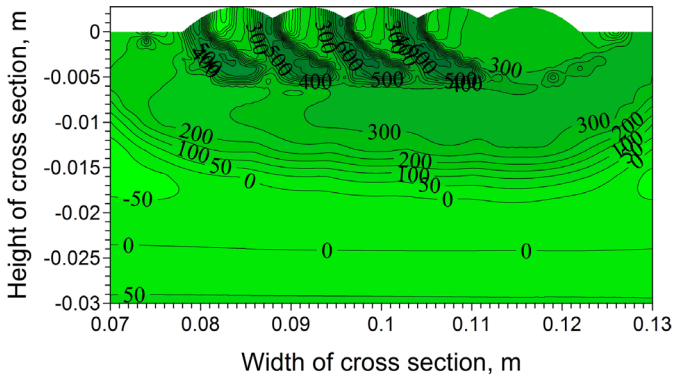

Fig. 24. Residual stress distribution in the middle part of cross section after the weld cooling

Stress distributions are characterized by high values of tensile stress in the area of welds and heat affected zone. Compressive stresses dominate in parent material zone (outside the HAZ). Residual stresses in the zone outside the HAZ have a uniform linear distribution in relation to section height: from compressive stresses of approx. 205 MPa at the upper surface of the plate to the tensile stresses of approx. 55 MPa at the bottom surface.

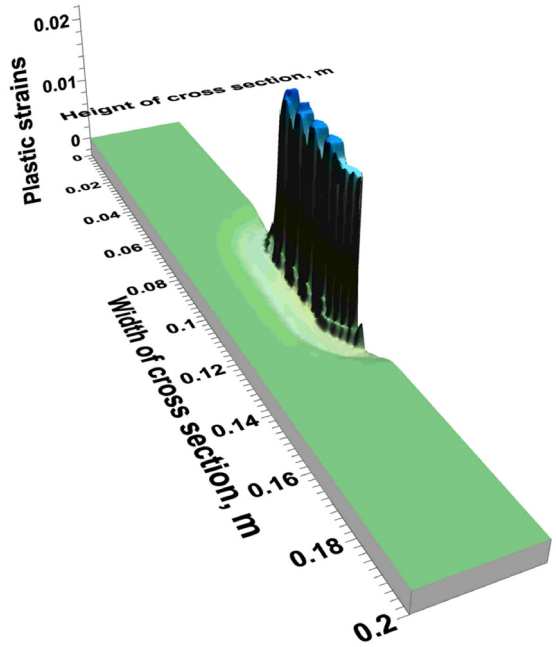

Fig. 25. Plastic strain distribution in the whole cross section of the plate

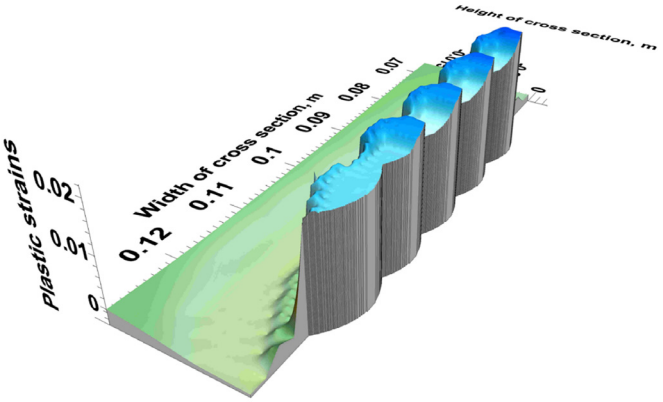

Fig. 26. Plastic strain distribution in the middle part of cross section of the plate

Figures 27-29 illustrate stress state changes and plastic strains at individual points of the section. These stresses result from thermal and structural strains (comp. Fig. 12) and plastic strains. They depend on the tensile curves as a function of temperature and phase composition (comp. Figs. 6 and 9), and on section forces which meet the conditions of stress balance.

In point 1 (Figs. 27,28) while applying the first weld, stress state is mainly determined by thermal strains, and during the application of the second, third and fourth welds by both thermal and structural strains arising during phase transformations of heating and cooling. During the fifth bead, thermal strains are again the cause of changes in stress state. The expansion of the material during the heating causes the compression, and during cooling shrinkage of the material causes tensile stresses.

At point *2* (Figs. 29,30) during padding of the first and second beads the stresses are the effect of thermal strains, moreover the plastic deformation in the second bead gave rise to tensile stresses of nearly 300 MPa. When performing the third and fourth

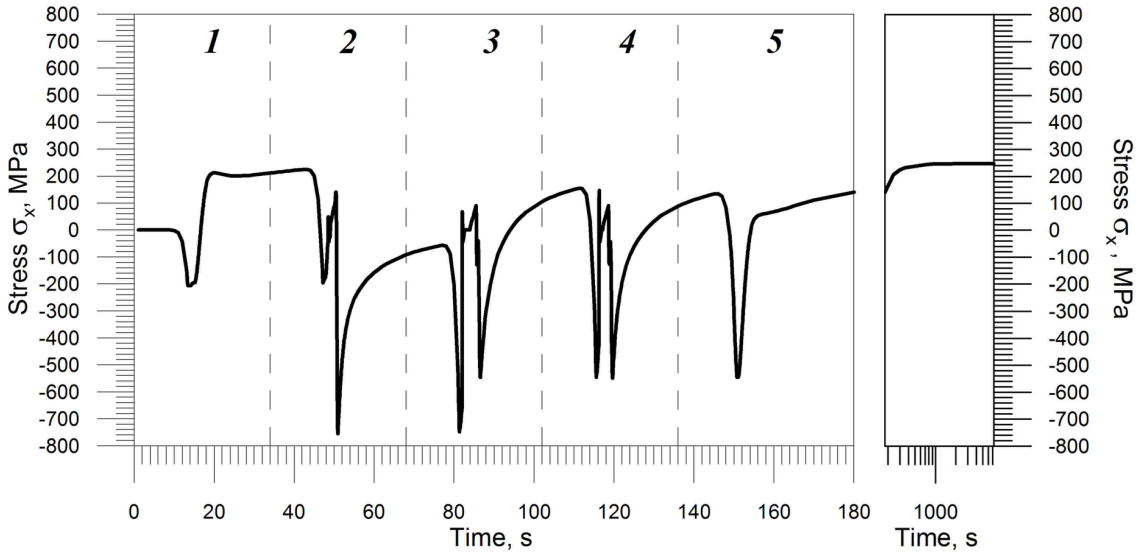

Fig. 27. Stresses during surfacing at point 1

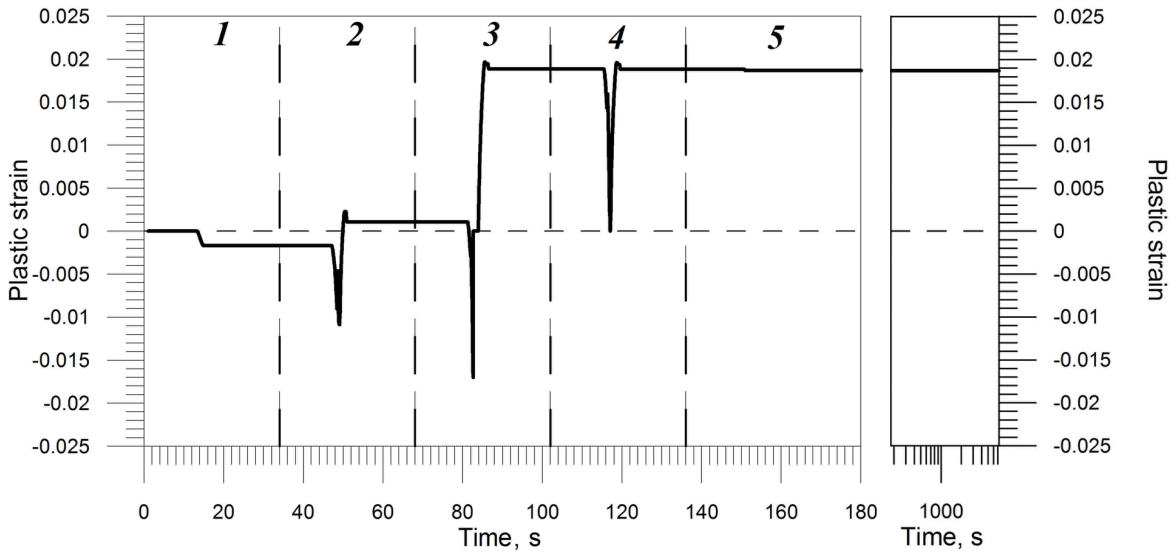

Fig. 28. Plastic strains during surfacing at point 1

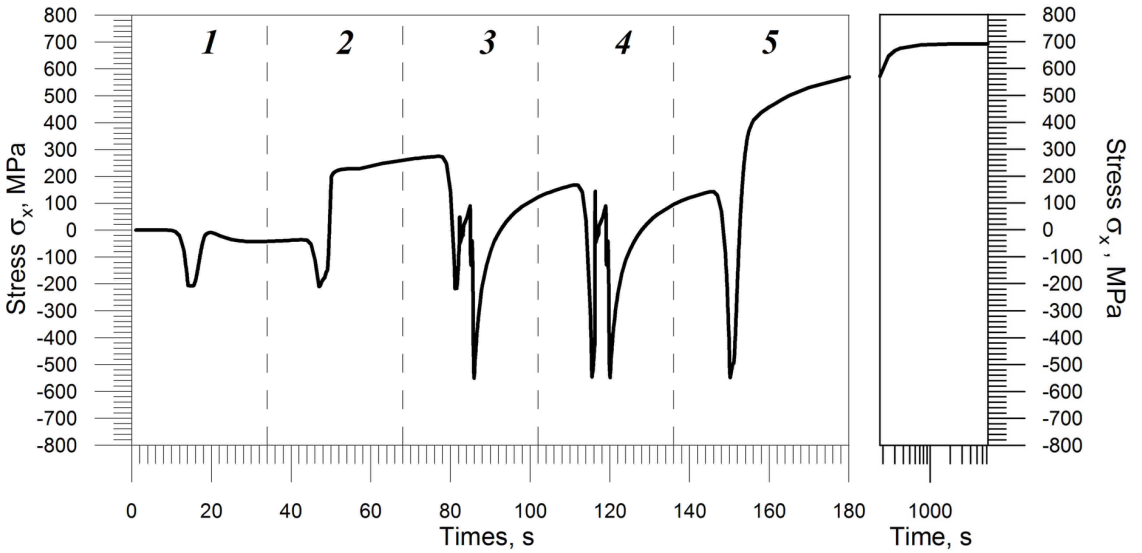

Fig. 29. Stresses during surfacing at point 2

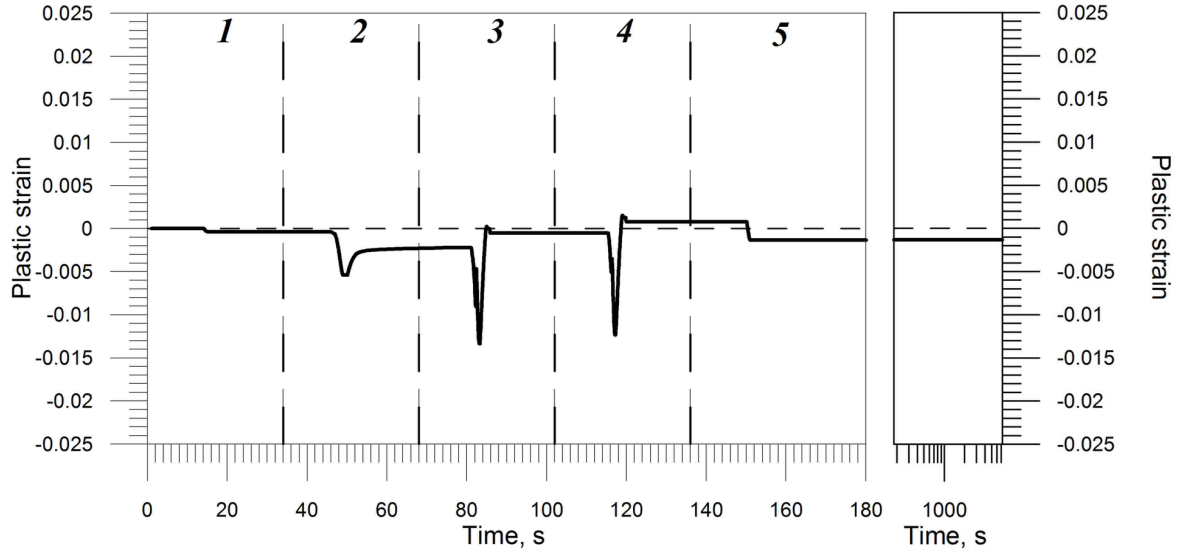

Fig. 30. Plastic strains during surfacing at point 2

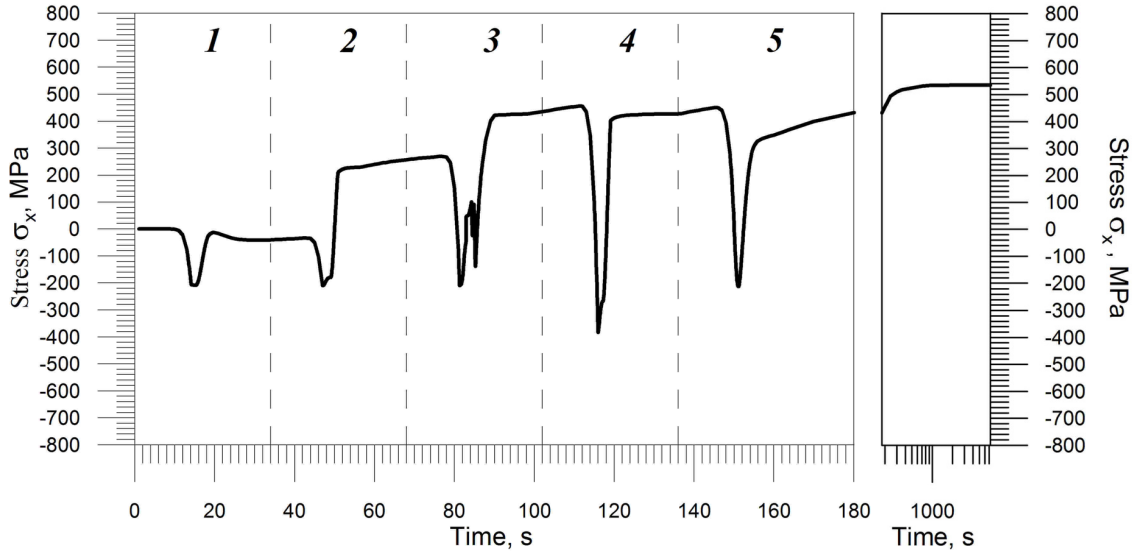

Fig. 31. Stresses during surfacing at point 3

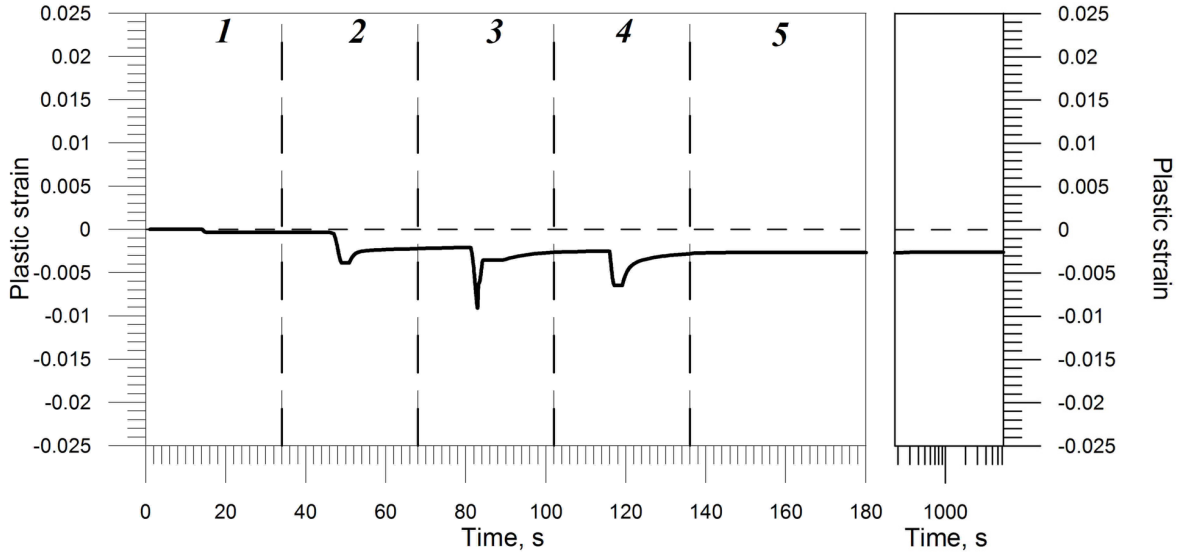

Fig. 32. Plastic strains during surfacing at point 3

welds, during heating austenitic transformations occur, then melting takes place (stresses drop to zero). After solidification cooling transformations occur causing a series of abrupt stress changes reflected in the charts by faults. In the course of the fifth bead, first the material expands causing a decrease in stresses. Then, while cooling, the material shrinks causing a reduction of compressive stresses and later evoking the formation and development of tensile stress.

In point 3 (Figs. 31, 32) in the partial transformation zone, stress states are largely determined by the rising plastic strains in successive thermal cycles (beads), by stress equilibrium of cross section and by thermal strains. Only during the fourth weld, structural strains occurring during a partial austenitic transformation and then during the formation of ferrite, pearlite and bainite from overcooled austenite cause abrupt stress changes.

7. Conclusions

Proposed in the work model allows one for full analysis of thermomechanical states during multipass weld surfacing. It takes into account relevant interactions between fields: temperature, phase transformation and stress.

In case of large (of a few hundred degrees) temperature changes and phase transformation proceeding at a given point, stress changes are mainly determined by thermal and structural strains, and in the case of relatively small changes in temperature a dominant role is played by stresses which result from stress equilibrium of the cross section (thermal loads of other areas).

Complex thermal cycles in case of multipass weld surfacing cause repeatedly occurring phase transformations. Temperature changes and phase transformations result in heat affected zone numerous and significant strain changes, which is reflected in stress states. Performing successive beads causes significant changes in volumetric share of particular structures and varied values of these shares in the next welds. The complicated temperature history, volumetric phase participations and thermal and structural strains result in stress fields with high gradient, which are changing dynamically during subsequent heat source passes.

Stress distributions are characterized by high values of tensile stresses in welds and heat affected zone. In parent material zone (outside the HAZ) compressive stresses dominate and have a uniform linear distribution with respect to the section height: from compression stresses at the upper surface of the plate to the tensile stresses at the bottom surface.

REFERENCES

[1] L.E. Lindgren, H. Runnemalm, M.O. Näsström, Simulation of multipass welding of a thick plate, Int. J. Num. Meth. Eng. **44**, 1301-1316 (1999).

[2] W. Jiang, K. Yahiaoui, F.R. Hall, T. Laoui, Finite element simulation of multipass welding: full three-dimensional versus generalized plane strain or axisymmetric models, J. Strain Analysis **40**, 587-597 (2005).

[3] D. Deng, H. Murakawa, Prediction of welding residual stress in multi-pass butt-welded modified 9Cr-1Mo steel pipe considering phase transformation effects, Comput. Mater. Sci. **37**, 209-219 (2006).

[4] W. Jiang, Z. Liu, J.M. Gong, S.T. Tu, Finite element analysis of the effect of welding heat input and layer number on residual stress in repair welds stainless steel clad plate, Mater. Des. **32**, 2851-2857 (2011).

[5] C. Heinze, C. Schwenk, M. Rethmeier, Numerical calculation of residual stress development of multi-pass gas metal arc welding under high restraint conditions. Mater. Des. **35**, 201-209 (2012).

[6] S. Joshi, J. Hildebrand, A.S. Aloraier, T. Rabczuk, Characterization of material properties and heat source parameters in welding simulation of two overlapping beads on a substrate plate, Comp. Mater. Sci. **69**, 559-565 (2013).

[7] L. Börjesson, L.E. Lindgren, Simulation of multipass welding with simultaneous computation of material properties, Trans. ASME **123**, 106-111 (2001).

[8] L.E. Lindgren, E. Hedblom, Modelling of addition of filler material in large deformation analysis of multipass welding, Commun. Numer. Meth. En. **17**, 647-657 (2001).

[9] A. Kulawik, Modeling of thermomechanical phenomena of welding process of steel pipe, Arch. Metal. Mater. **57**, 1229-1238 (2012).

[10] J. Winczek, Analytical solution to transient temperature field in a half-infinite body caused by moving volumetric heat source, Int. J. Heat Mass Transfer **53**, 5774-5781 (2010).

[11] J. Winczek, New approach to modeling of temperature field in surfaced steel elements, Int. J. Heat Mass Transfer **54**, 4702-4709 (2011).

[12] J. Winczek, Modelling of temperature field and phase transformations in weld rebuilding elements. Informatics in Materials Technology **2** (4), 121-137 (2004).

[13] W. Piekarska, M. Kubiak, A. Bokota, Numerical simulation of thermal phenomena and phase transformations in laser-arc hybrid welded joint, Arch. Metal. Mater. **56**, 409-421 (2011).

[14] J. Winczek, Modeling of heat affected zone in multipass GMAW surfacing S235 steel element, Proc. Eng. **136**, 108-113 (2016).

[15] M. Avrami, M., Kinetics of phase change. I. General theory, J. Chem. Physics **7**, 1103-1112 (1939).

[16] R. Parkitny, J. Winczek, Modelling of phase transformations during multipass surfacing, In:. Conf. Proc. XXXVIII Sympozjon Modelling in Mechanics, Silesian University of Technology, Gliwice 219-224 (1999).

[17] T. Domański, A. Bokota, Numerical models of hardening phenomena of tools steel base on the TTT and CCT diagrams, Archiv. Metal.Mater. **56**, 325-344 (2011).

[18] J. Winczek, K. Makles, M. Gucwa, R. Gnatowska, M. Hatala, Modelling of strains during SAW surfacing taking into heat of the weld in temperature field description and phase transformations, IOP Conf. Series: Materials Science and Engineering 225 (2017) 012038 doi:10.1088/1757-899X/225/1/012038 (2017).

[19] J. Winczek, The analysis of stress states in steel rods surfaced by welding, Arch. Metal. Mater. **58**, 1243-1252 (2013).

[20] J. Brózda, J. Pilarczyk, M. Zeman, TTT-welding diagrams transformation of austenite, Śląsk, Katowice 1983.

[21] J. Winczek, A. Kulawik, Dilatometric and hardness analysis of C45 steel tempering with different heating-up rates, Metalurgija **51** (1), 9-12 (2012).

[22] J. Gawąd, D. Szeliga, A. Bator, V. Pidvysockyy, M. Pietrzyk, Interpretation of the tensile test results interpretation based on two criterion optimization, In: Proc. 14. Conf. KomPlasTech, Informatics in Metal Technology, ed. M. Pietrzyk et al., Akapit, Cracow, 27-34 (2004).

[23] P.M.M. Vila Real, R. Cazeli, L. Simoes da Silva, A. Santiago, P. Piloto, The effect of residual stresses in the lateral-torsional buckling of steel I-beams at elevated temperature, J. Constr. Steel Res. **60**, 783-793 (2004).

[24] M. Melander, A Computional and Experimental Investigation of Induction and Laser Hardening, Linkoping Studies in Science and Technology, Dissertation No 124, Linkoping Univeristy (1985).

[25] J. Lian, Z. Jiang, J. Liu, Theoretical model for the tensile work hardening behaviour of dual-phase steel, Mater. Sci. Eng. **A147**, 55-65 (1991).

[26] S.K. Kim, Y.M. Kim, Y.J. Lim, N.J. Kim N.J., Relationship between yield ratio and the material constants of the swift equation, Metals Materials Int. **12**, (2), 131-135 (2006).